Virial series expansion and Monte Carlo studies of equation of state for hard spheres in narrow cylindrical pores

K. K. Mon*

Department of Physics and Astronomy, University of Georgia, Athens, Georgia 30602, USA

(Received 4 January 2018; published 14 May 2018)

In this paper, the virial series expansion and constant pressure Monte Carlo method are used to study the longitudinal pressure equation of state for hard spheres in narrow cylindrical pores. We invoke dimensional reduction and map the model into an effective one-dimensional fluid model with interacting internal degrees of freedom. The one-dimensional model is extensive. The Euler relation holds, and longitudinal pressure can be probed with the standard virial series expansion method. Virial coefficients B_2 and B_3 were obtained analytically, and numerical quadrature was used for B_4. A range of narrow pore widths ($2R_p$), $R_p < (\sqrt{3}+2)/4 = 0.9330\ldots$ (in units of the hard sphere diameter) was used, corresponding to fluids in the important single-file formations. We have also computed the virial pressure series coefficients B_2', B_3', and B_4' to compare a truncated virial pressure series equation of state with accurate constant pressure Monte Carlo data. We find very good agreement for a wide range of pressures for narrow pores. These results contribute toward increasing the rather limited understanding of virial coefficients and the equation of state of hard sphere fluids in narrow cylindrical pores.

DOI: 10.1103/PhysRevE.97.052114

I. INTRODUCTION

The thermodynamics of fluids in narrow pores and the crossovers from the one-dimensional limit has been a subject of long-standing interest [1–13], but much more remains basically unsolved. In this paper, we use the virial expansion method to study hard sphere fluid in very narrow cylindrical pores. Virial expansion has been used extensively to study interacting fluids [14–19]. For the bulk fluids, many virial coefficients [14–19] can be evaluated. This is especially true for hard sphere fluids. Analytical results have been obtained in low and high dimensions for hard spheres [14–24]. There is also much interest in applications of virial series expansions to inhomogeneous fluids with surfaces and walls [25].

The second virial coefficient for hard disks in narrow hard channels has been computed analytically [9,11,12]. For homogeneous fluids in very narrow cylindrical pores, much less is known. There are some numerical results for the second virial coefficients for hard spheres in cylindrical pores [9]. The third and fourth virial coefficients of hard spheres in cylindrical pores are basically unexplored. In this paper we have evaluated them. Virial coefficients B_2 and B_3 were obtained analytically, and numerical quadrature was used for B_4. A range of narrow pore widths ($2R_p$), $R_p < (\sqrt{3}+2)/4 = 0.9330\ldots$ (in units of the hard sphere diameter) was used, corresponding to fluids in the important single-file formations. They correspond to three-dimensional single-file fluids with only nearest-neighbor interactions and are of some interest [26].

We have also computed the virial pressure series coefficients B_2', B_3', and B_4' to compare a truncated virial pressure series equation of state with accurate constant pressure Monte Carlo data. We find very good agreement for a wide range of pressures for narrow pores. These results contribute toward increasing the rather limited understanding of virial coefficients and equation of state of hard sphere fluids in narrow cylindrical pores.

In Sec. II, the Euler relation, dimensional reduction, and method of virial expansion for hard spheres in cylindrical pores will be discussed. Computational techniques are considered in Sec. III. The virial expansion equations of state are compared to accurate Monte Carlo data in Sec. IV, and the paper ends with some remarks in Sec. V.

II. DIMENSIONAL REDUCTION, EULER RELATION, AND VIRIAL SERIES EXPANSION

In this section, we will review the dimensional reduction analysis to show that fluids in narrow cylindrical pores can be reduced to an effectively one-dimensional fluid model. It is extensive in the longitudinal length L, and the longitudinal pressure can be studied with standard virial series expansion method. We will take the dimensional reduction approach, related to that used in Ref. [4]; see also Ref. [2].

The hard spheres are in narrow cylindrical pores with the length of the pore taken to the thermodynamic limit ($N, L \to \infty$). The linear number density is fixed at $l^{-1} = N/L$. One starts by rewriting the partition function:

$$Q_N(V,T) = \frac{1}{N!\Lambda^{3N}} \int_0^L dz_1 \cdots \int_0^L dz_N \times \left\{ \int_0^{\hat{R}} r_1 dr_1 \int_0^{2\pi} d\theta_1 \cdots \int_0^{\hat{R}} r_N\, dr_N \int_0^{2\pi} d\theta_N \times \exp[-\beta U(r_1,\theta_1,z_1,\ldots,r_N,\theta_N,z_N)] \right\}$$

*kkmon@hal.physast.uga.edu

$$= \frac{1}{N!\Lambda^{3N}} \int_0^L dz_1 \cdots \int_0^L dz_N \times W_{\text{eff}}(\hat{R}, z_1, \ldots, z_N), \quad (1)$$

$$W_{\text{eff}}(\hat{R}, z_1, \ldots, z_N) = \left\{ \int_0^{\hat{R}} r_1\, dr_1 \int_0^{2\pi} d\theta_1 \cdots \int_0^{\hat{R}} r_N\, dr_N \times \int_0^{2\pi} d\theta_N \exp[-\beta U(r_1, \theta_1, z_1, \ldots, r_N, \theta_N, z_N)] \right\}. \quad (2)$$

$\hat{R} = R_p - \frac{1}{2}$ and Λ is the thermal de Broglie wavelength. Lengths are in units of the hard sphere diameter, $\sigma_{hs} = 1$, and U is the sum of nearest-neighbor hard sphere potentials. W_{eff} in general is complicated [4], but we do not need to evaluate it for our analysis.

For fixed $\hat{R}$, and constant linear number density $l^{-1} = N/L$, there is only one spatial extensive parameter L. The transverse lengths are fixed and do not scale with N. Thus, this model is one-dimensional and extensive in the longitudinal direction, and the pressure is anisotropic:

$$Q_N(V = \pi \hat{R}^2 L, T) = Q_N(L, \hat{R}, T) = Q_N(L, T). \quad (3)$$

It then follows from Euler's theorem that the longitudinal pressure P_L is related to the grand partition function Ξ as

$$\beta P_L = \frac{1}{V} \ln \Xi = \frac{1}{\pi \hat{R}^2 L} \ln \Xi, \quad (4)$$

and $\beta = 1/k_B T$. For the partition function, one can apply the Mayer cluster integral expansion method (see Ref. [14]) to obtain

$$\Xi(\mu, T, L) = \exp\left[\pi \hat{R}^2 L \sum_{k=0}^{\infty} \xi^k b_k(T) \right], \quad (5)$$

where $b_k(T)$ are the cluster integrals,

$$b_k(T) = \lim_{L\to\infty} \frac{1}{k! \pi \hat{R}^2 L} \int_V d^3\mathbf{r_1} \cdots d^3\mathbf{r_k} U_k(\mathbf{r_1}, \ldots, \mathbf{r_N}). \quad (6)$$

$U_k(\mathbf{r_1}, \ldots, \mathbf{r_N})$ are the Ursell functions defined as the sum of all connected numbered Mayer graphs of k points [14]. We have introduced the fugacity ξ in terms of absolute activity $\lambda = \exp(\beta\mu)$, chemical potential μ, and thermal de Broglie wavelength Λ:

$$\xi = \frac{\lambda}{\Lambda^3}. \quad (7)$$

This reduces to

$$\beta P_L = \sum_{k=0}^{\infty} \xi^k b_k(T). \quad (8)$$

.

In the grand ensemble, the average number of particles in the system is

$$N = k_B T \left. \frac{\partial ln\, \Xi}{\partial \mu} \right|_{V,T} = \lambda \left. \frac{\partial ln\, \Xi}{\partial \lambda} \right|_{V,T} = \pi \hat{R}^2 L \sum_{k=0}^{\infty} k \xi^k b_k(T). \quad (9)$$

The number density ρ is

$$\rho = \frac{N}{\pi \hat{R}^2 L} = \sum_{k=0}^{\infty} k \xi^k b_k(T). \quad (10)$$

A virial series for the longitudinal pressure βP_L in terms of density ρ can be introduced:

$$\beta P_L = \rho\left(1 + B_2^{(\rho)} \rho + B_3^{(\rho)} \rho^2 + B_4^{(\rho)} \rho^3 + \cdots\right). \quad (11)$$

To obtain the equation for the virial coefficients $B_n^{(\rho)}$, start by eliminating ρ with Eq. (10). Then equating it to Eq. (8) for βP_L will lead to

$$B_{k+1}^{(\rho)} = -\frac{k}{k+1} \beta_k, \quad (12)$$

where $B_{k+1}^{(\rho)}$ are the virial coefficients and β_k are the irreducible cluster integrals. For a good reference, see Ref. [14].

This shows that we can apply the standard virial series expansion method to study the longitudinal pressure P_L of fluids in cylindrical pores. Since the Euler relation does not hold for the transverse length scale, which is not extensive, the way to study the transverse pressure is different. It has to be computed by taking the appropriate derivative of the free energy and will be considered elsewhere.

Since $\hat{R}$ is a constant, ρ is related to l^{-1} as

$$\rho = \frac{N}{\pi \hat{R}^2 L} = \frac{1}{\pi \hat{R}^2} \frac{N}{L} = \frac{1}{\pi \hat{R}^2} l^{-1}. \quad (13)$$

Now Eq. (11) can be rewritten as a virial expansion for a one-dimensional system with linear density l^{-1}:

$$\beta p = l^{-1}(1 + B_2 l^{-1} + B_3 l^{-2} + B_4 l^{-3} + \cdots). \quad (14)$$

$p = P_L \pi \hat{R}^2$ is the linear pressure for the equivalent one-dimensional system with one-dimensional density virial expansion coefficients B_n defined by

$$B_n = \frac{B_n^{(\rho)}}{(\pi \hat{R}^2)^{n-1}}. \quad (15)$$

III. EVALUATION OF VIRIAL COEFFICIENTS: B_2, B_3, B_4

There are some numerical estimates [9] for the B_2, but no virial coefficients of hard spheres in cylindrical pores are known to have been calculated analytically. We have evaluated B_2 and B_3 analytically. Parts of the multi-integrals can be done in closed form and the remaining by expanding in a power series and integrating term by term analytically.

The second virial coefficient in the ρ series expansion is

$$B_2^{(\rho)} = \frac{-1}{2V} \int dv_1 \int dv_2 f_{12} = \frac{-1}{2V} \int_0^{\hat{R}} r_1\, dr_1 \int_0^{2\pi} d\theta_1 \times \int_0^{\hat{R}} r_2\, dr_2 \int_0^{2\pi} d\theta_2 \int_0^L dz_1 \int_0^L dz_2 f_{12}.$$
$$= \frac{-2\pi}{2(\pi \hat{R}^2)} \int_0^{2\pi} d\theta_{12} \int_0^{\hat{R}} r_1\, dr_1 \int_0^{\hat{R}} r_2\, dr_2 \int_{-1}^{1} dz_{12} f_{12} \quad (16)$$

with

$$f_{12} \equiv f_{12}(r_{12}) = e^{-\beta V_{hs}(r_{12})} - 1. \quad (17)$$

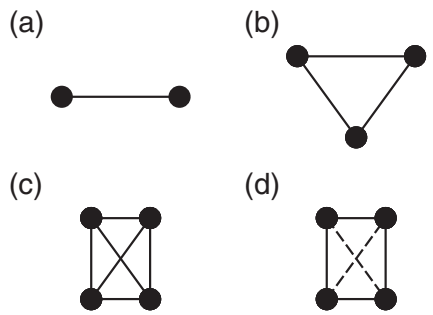

FIG. 1. Ree-Hoover diagrams for virial coefficients. (a) B_2, (b) B_3, (c) $\tilde{S}_1$ for B_4, (d) $\tilde{S}_2$ for B_4. The solid lines denote the Mayer f_{ij} function, and dashed lines denote $\tilde{f}_{ij} = 1 + f_{ij}$.

$\hat{R} = R_p - \frac{1}{2}, \theta_{12} = |\theta_1 - \theta_2|$, $r_{12} = |\vec{r}_1 - \vec{r}_2| = \sqrt{z_{12}^2 + r_1^2 + r_2^2 - 2r_1 r_2 \cos(\theta_{12})}$, and $V_{hs}(r_{12})$ is the hard sphere potential.

Then, the one-dimensional virial expansion coefficients for B_2 is

$$B_2 = \frac{B_2^{(\rho)}}{(\pi \hat{R}^2)} = \frac{-2\pi}{2(\pi \hat{R}^2)^2} \int_0^{2\pi} d\theta_{12} \times \int_0^{\hat{R}} r_1 dr_1 \int_0^{\hat{R}} r_2\, dr_2 \int_{-1}^{1} dz_{12} f_{12}. \tag{18}$$

This corresponds to the Ree-Hoover diagram [18] of Fig. 1(a).

The integration over z_{12} is elementary,

$$\int_{-1}^{1} dz_{12} f_{12} = -2\sqrt{1 - \epsilon_{12}(r_1, r_2, \theta_{12})}, \tag{19}$$

with

$$\epsilon_{ij}(r_i, r_j, \theta_{ij}) = [r_i^2 + r_j^2 - 2r_i r_j \cos(\theta_{ij})]. \tag{20}$$

One can expand the $\sqrt{1 - \epsilon_{12}}$ in a power series of ϵ_{12}:

$$\sqrt{1 - \epsilon_{12}} = \sum_{n=0}^{\infty} \frac{(2n)!}{(1 - 2n)(n!)^2 (4^n)} (\epsilon_{12})^n. \tag{21}$$

Each term can be integrated exactly to yield a power series in powers of $\hat{R}$ with

$$\begin{aligned} B_2(\hat{R}) = 1 &- \frac{1}{2}\hat{R}^2 - \frac{5}{24}\hat{R}^4 - \frac{7}{32}\hat{R}^6 - \frac{21}{64}\hat{R}^8 - \frac{77}{128}\hat{R}^{10} \\ &- \frac{1287}{1024}\hat{R}^{12} - \frac{23\,595}{8192}\hat{R}^{14} - \frac{347\,633}{49\,152}\hat{R}^{16} - \frac{600\,457}{32\,768}\hat{R}^{18} - \frac{6\,495\,853}{131\,072}\hat{R}^{20} \\ &- \frac{218\,360\,597}{1\,572\,860}\hat{R}^{22} - \frac{419\,924\,225}{1\,048\,576}\hat{R}^{24} - \frac{2\,483\,551\,845}{2\,097\,152}\hat{R}^{26} - \frac{120\,038\,339\,175}{33\,554\,432}\hat{R}^{28} \\ &- \frac{5\,910\,122\,934\,675}{536\,870\,912}\hat{R}^{30} - \frac{36\,967\,239\,532\,575}{1\,073\,741\,824}\hat{R}^{32} - \frac{234\,558\,215\,747\,625}{2\,147\,483\,648}\hat{R}^{34} \cdots . \end{aligned} \tag{22}$$

More terms can be easily calculated with the help of symbolic computations. Convergence is rapid, and we have checked it with numerical integrations. For example, with $\hat{R} = 0.4$, Eq. (22) yields 0.91345843 versus 0.91345844 from numerical quadrature. The uncertainty is in the last digit.

The third virial coefficient also has only one Ree-Hoover diagram [Fig. 1(b)]:

$$B_3^{(\rho)} = \frac{-1}{3V} \int dv_1 \int dv_2 \int dv_3 f_{12} f_{13} f_{23} \tag{23}$$

and

$$B_3 = \frac{-2\pi}{3(\pi \hat{R}^2)^3} \int_0^{2\pi} d\theta_{12} \int_0^{2\pi} d\theta_{13} \int_0^{\hat{R}} r_1 dr_1 \int_0^{\hat{R}} r_2\, dr_2 \int_0^{\hat{R}} r_3\, dr_3 \times \int_{-1}^{1} dz_{12} f_{12} \int_{-1}^{1} dz_{13} f_{13} f_{23}, \tag{24}$$

where $\theta_{ij} = |\theta_i - \theta_j|$, $r_{ij} = |\vec{r}_i - \vec{r}_j| = \sqrt{z_{ij}^2 + r_i^2 + r_j^2 - 2r_i r_j \cos(\theta_{ij})}$.

The integrations over z_{12}, z_{13} can be done analytically and denoted as $-\mathbf{A}$:

$$-\mathbf{A} \equiv \int_{-1}^{1} dz_{12} f_{12} \int_{-1}^{1} dz_{13} f_{13} f_{23}, \tag{25}$$

$$\mathbf{A} = 2(\sigma_c \sigma_b + \sigma_a \sigma_c + \sigma_a \sigma_b) - \left(\sigma_a^2 + \sigma_b^2 + \sigma_c^2\right), \tag{26}$$

$$\sigma_a = \sigma_{12}, \quad \sigma_b = \sigma_{13}, \sigma_c = \sigma_{23}, \tag{27}$$

$$\sigma_{ij} = \sqrt{1 - \epsilon_{ij}}, \tag{28}$$

and

$$B_3 = \frac{2\pi}{3(\pi \hat{R}^2)^3} \int_0^{2\pi} d\theta_{12} \int_0^{2\pi} d\theta_{13} \int_0^{\hat{R}} r_1\, dr_1 \int_0^{\hat{R}} r_2\, dr_2 \int_0^{\hat{R}} r_3\, dr_3 \times \left[2(\sigma_c\sigma_b + \sigma_a\sigma_c + \sigma_a\sigma_b) - \left(\sigma_a^2 + \sigma_b^2 + \sigma_c^2\right)\right]. \tag{29}$$

By symmetry, there are only two types of integrals to do:

$$\mathbf{B} = \int_0^{2\pi} d\theta_{12} \int_0^{2\pi} d\theta_{13} \int_0^{\hat{R}} r_1\, dr_1 \int_0^{\hat{R}} r_2\, dr_2 \int_0^{\hat{R}} r_3\, dr_3 \sigma_\alpha \sigma_\beta, \quad \alpha \neq \beta, \tag{30}$$

$$\mathbf{C} = \int_0^{2\pi} d\theta_{12} \int_0^{2\pi} d\theta_{13} \int_0^{\hat{R}} r_1\, dr_1 \int_0^{\hat{R}} r_2\, dr_2 \int_0^{\hat{R}} r_3\, dr_3 (\sigma_\alpha)^2. \tag{31}$$

C can be evaluated in closed form as

$$\mathbf{C} = \frac{\pi^2 \hat{R}^6}{2}(1 - \hat{R}^2). \tag{32}$$

The **B** term appears to be different and has to be calculated as for B_2 by expanding the $\sqrt{\cdots}$ and integrate term by term to yield a power series in $\hat{R}$. The final result for B_3 is

$$\begin{aligned} B_3(\hat{R}) = 1 &- \hat{R}^2 - \frac{7}{24}\hat{R}^4 - \frac{19}{48}\hat{R}^6 - \frac{65}{96}\hat{R}^8 - \frac{1291}{960}\hat{R}^{10} \\ &- \frac{6073}{2048}\hat{R}^{12} - \frac{1\,822\,885}{258\,048}\hat{R}^{14} - \frac{3\,072\,455}{172\,032}\hat{R}^{16} - \frac{13\,960\,009}{294\,912}\hat{R}^{18} - \frac{2\,306\,857\,403}{17\,694\,720}\hat{R}^{20} \\ &- \frac{3\,206\,519\,887}{8\,650\,752}\hat{R}^{22} - \frac{18\,728\,895\,875}{17\,301\,504}\hat{R}^{24} - \frac{88\,185\,547\,953}{27\,262\,976}\hat{R}^{26} - \frac{361\,234\,293\,689\,153}{36\,641\,439\,744}\hat{R}^{28} \\ &- \frac{287\,223\,536\,237\,301}{9\,395\,240\,960}\hat{R}^{30} - \frac{155\,026\,303\,764\,017}{1\,610\,612\,736}\hat{R}^{32} - \frac{33\,641\,701\,357\,295\,089}{109\,521\,666\,048}\hat{R}^{34} \\ &- \frac{434\,647\,739\,535\,045\,095}{438\,086\,664\,192}\hat{R}^{36} - \frac{1\,057\,439\,817\,596\,234\,513}{326\,417\,514\,496}\hat{R}^{38} \cdots . \end{aligned} \tag{33}$$

Again, more terms can be easily calculated with the help of symbolic computations. Convergence is also rapid, and we have checked it with numerical integrations. For example, with $\hat{R} = 0.4$, Eq. (33) yields 0.830244942 versus 0.830248 from numerical quadrature. The uncertainty is in the last digit for the numerical integration. The terms decreases rapidly, and the last term shown in Eq. (33) contributes a small value of 0.000000002.

The fourth virial coefficient has two Ree-Hoover diagrams. The first diagram $\tilde{S}_1$ [Fig. 1(c)] contributes:

$$\begin{aligned} B_{4a} = \frac{2\pi}{4(\pi \hat{R}^2)^4} &\int_0^{2\pi} d\theta_{12} \int_0^{2\pi} d\theta_{13} \int_0^{2\pi} d\theta_{14} \\ &\times \int_0^{\hat{R}} r_1\, dr_1 \int_0^{\hat{R}} r_2\, dr_2 \int_0^{\hat{R}} r_3\, dr_3 \int_0^{\hat{R}} r_4\, dr_4 \\ &\times \int_{-1}^{1} f_{12}\, dz_{12} \int_{-1}^{1} f_{13} f_{23}\, dz_{13} \int_{-1}^{1} f_{14} f_{24} f_{34}\, dz_{14}. \end{aligned} \tag{34}$$

The second Ree-Hoover diagram $\tilde{S}_2$ [Fig. 1(d)] is denoted as B_{4b}. In these diagrams, the solid lines denote the Mayer f_{ij} functions, and dashed lines denote $\tilde{f}_{ij} = 1 + f_{ij}$. Both diagrams contribute to $B_4 = B_{4a} + B_{4b}$:

$$\begin{aligned} B_{4b} = -\frac{3}{8}\left[\frac{2\pi}{(\pi \hat{R}^2)^4}\right] &\int_0^{2\pi} d\theta_{12} \int_0^{2\pi} d\theta_{13} \int_0^{2\pi} d\theta_{14} \\ &\times \int_0^{\hat{R}} r_1\, dr_1 \int_0^{\hat{R}} r_2\, dr_2 \int_0^{\hat{R}} r_3\, dr_3 \int_0^{\hat{R}} r_4\, dr_4 \\ &\times \int_{-1}^{1} f_{12}\, dz_{12} \int_{-1}^{1} \tilde{f}_{13} f_{23}\, dz_{13} \int_{-1}^{1} f_{14} \tilde{f}_{24} f_{34}\, dz_{14}. \end{aligned} \tag{35}$$

For now, we are not able to reduce the B_4 calculations to be suitable for symbolic computations. To provide estimates which will be useful for future analytical calculations, we have used numerical Gaussian integrations [27] for nine different values of $\hat{R}$. See Table I. The number of Gaussian integration points used for each integral($\leqslant 1000$) was varied and extrapolated to the large number limits. We have checked our numerical method by using the same routines to obtain estimates for B_2 and B_3. As noted above, they are in good agreement with our analytic results.

We have also computed the virial pressure series coefficients B_2', B_3', and B_4' to compare a truncated virial pressure series equation of state with accurate constant pressure Monte Carlo

TABLE I. Second, third, and fourth virial coefficients for hard spheres in cylindrical pores with widths $2R_p$. $R_p = \frac{1}{2}$ is the exactly soluble hard rod model [28], and all virial coefficients are 1. For $R_p > \frac{1}{2}$, B_2, B_3 are analytic predictions of Eqs. (22) and (23), respectively. B_4 are extrapolated values from numerical integrations with $B_4 = B_{4a} + B_{4b}$. For B_4, the last two digits are uncertain. The magnitude of the uncertainties are in parentheses. The pressure virial series B_3', B_4' from Eqs. (40) and (39), respectively, are also shown.

R_p	B_2	B_3	B_3'	B_4	B_4'
$\frac{1}{2}$	1	1	0	1	0
0.52	0.999799966...	0.99959995...	−0.00000002...	0.9993130 (10)	−0.000000 (01)
0.55	0.998748694...	0.99749817...	−0.00000078...	0.9962235 (06)	−0.000000 (01)
0.60	0.994978944...	0.98997043...	−0.00001267...	0.9849752 (05)	−0.000000 (01)
0.65	0.988641951...	0.97734765...	−0.00006525...	0.9661182 (15)	−0.000000 (02)
0.70	0.979651759...	0.95950611...	−0.00021145...	0.9395689 (15)	−0.000000 (02)
0.75	0.967877124...	0.93625221...	−0.00053391...	0.9051441 (10)	−0.000000 (01)
0.80	0.953127105...	0.90729455...	−0.00115672...	0.8625625 (30)	−0.000000 (03)
0.85	0.935125123...	0.87219166...	−0.00226733...	0.8113642 (30)	−0.000004 (03)
0.90	0.913458430...	0.83024494...	−0.00416136...	0.7507733 (10)	−0.000018 (01)

data. The virial pressure series is defined as

$$\beta pl = 1 + B_2'(\hat{R})(\beta p) + B_3'(\hat{R})(\beta p)^2 + B_4'(\hat{R})(\beta p)^3 + \cdots . \tag{36}$$

The virial pressure series coefficients B_n' has been tabulated [29] in terms of the virial density series coefficients B_n:

$$B_2' = B_2, \tag{37}$$

$$B_3' = B_3 - B_2^2, \tag{38}$$

$$B_4' = B_4 - 3B_2B_3 + 2B_2^3. \tag{39}$$

See Ref. [29]. Note that $B_2'(\hat{R})$ is given by $B_2(\hat{R})$.

Using our analytic results for B_2, B_3 [Eqs. (22) and (23)], analytic predictions for B_3' are

$$\begin{aligned} B_3'(\hat{R}) = &-\frac{1}{8}\hat{R}^4 - \frac{1}{6}\hat{R}^6 - \frac{163}{576}\hat{R}^8 - \frac{359}{640}\hat{R}^{10} - \frac{2535}{2048}\hat{R}^{12} - \frac{47653}{16128}\hat{R}^{14} \\ &- \frac{429\,469}{57\,344}\hat{R}^{16} - \frac{1\,467\,523}{73\,728}\hat{R}^{18} - \frac{486\,331\,999}{8\,847\,360}\hat{R}^{20} - \frac{533\,012\,339\,566\,313}{3\,401\,605\,447\,680}\hat{R}^{22} - \frac{2\,080\,614\,548\,599\,833}{4\,535\,473\,930\,240}\hat{R}^{24} \\ &- \frac{5\,891\,402\,846\,511\,563}{4\,288\,084\,443\,136}\hat{R}^{26} - \frac{60\,459\,844\,952\,626\,018\,709}{14\,407\,963\,728\,936\,960}\hat{R}^{28} - \frac{602\,079\,763\,789\,143\,851}{46\,179\,370\,926\,080}\hat{R}^{30} \\ &- \frac{78\,132\,278\,795\,739\,354\,607}{1\,899\,951\,260\,958\,720}\hat{R}^{32} - \frac{471\,758\,329\,329\,931\,494\,447}{3\,588\,796\,826\,255\,360}\hat{R}^{34} - \frac{592\,546\,736\,554\,605\,787}{525\,702\,660\,096}\hat{R}^{36} \\ &- \frac{1\,278\,656\,698\,262\,280\,803\,109\,947}{385\,056\,788\,887\,633\,920}\hat{R}^{38} \cdots . \end{aligned} \tag{40}$$

As noted before, more terms can be easily generated as needed. Values for B_3', B_4' have been added to Table I. For values of B_4' that are small and within their uncertainties, we have listed them as $-0.000000(01)$ with uncertainty of the last two digits indicated in $(\cdots)$.

IV. TRUNCATED VIRIAL SERIES EQUATION OF STATE

We now have $[B_2(R_p), B_3(R_p), B_4(R_p)]$ and $[B_2'(R_p'), B_3'(R_p), B_4'(R_p)]$, to be used in truncated density virial series and pressure virial series, respectively. They can be employed to study the equation of state and probe the question of which truncated series is more accurate with the same number of coefficients. To provide benchmarks for this comparison, we have used extensive constant-pressure Monte Carlo simulations to provide accurate data. The constant pressure Monte Carlo method used is standard and well documented [30]. We have taken great care to account for the finite number of particles used by using a range of number of particles and very long runs to ensure convergence. For each pressure, we used up to 3000 hard spheres and extrapolate the finite-size dependences to the large N limit. The number of configurations sampled can be as long as 10^{11} Monte Carlo steps per particle. Typically 24 separate runs are used to estimate statistical errors. Our results are consistent with previous published data of limited accuracy [9].

In Figs. 2–4 we compare pressure virial and density virial series expansions to Monte Carlo data, denoted by a $\times$. The statistical errors are less than the size of the symbols. Results for three different values of pore radii R_p are shown. They range from $R_p = 0.52$ very close to the one-dimensional limit of 0.5 to $R_p = 0.90$ far from the one-dimensional limit. For

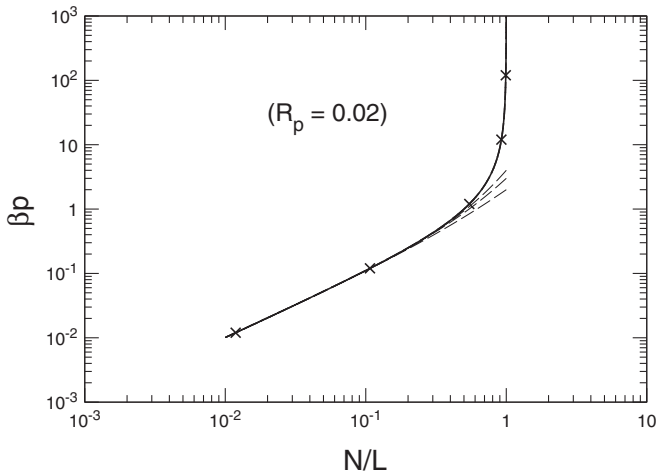

FIG. 2. Comparisons of linear pressure versus linear density plot for pore radius of $R_p = 0.52$ with Monte Carlo data. Monte Carlo data are denoted by a $\times$, and the statistical errors are less than the size of the symbols. The truncated virial density series are denoted by three dashed lines. The lowest line has $n_{max} = 2$, then $n_{max} = 3$ and $n_{max} = 4$. n_{max} is the maximum order of virial coefficients used in the truncated series. The truncated virial pressure series are denoted similarly by dotted, dashed, and solid lines. The lines for the three different pressure series are very close to each other and not distinguishable in the plots. A more quantitative comparison is given in Table II.

each pore radius, two sets of truncated series expansion predictions are plotted. The maximum order of the truncated series used is denoted by n_{max}. The density series are shown as three dashed lines. The lowest line has $n_{max} = 2$, then $n_{max} = 3$ and

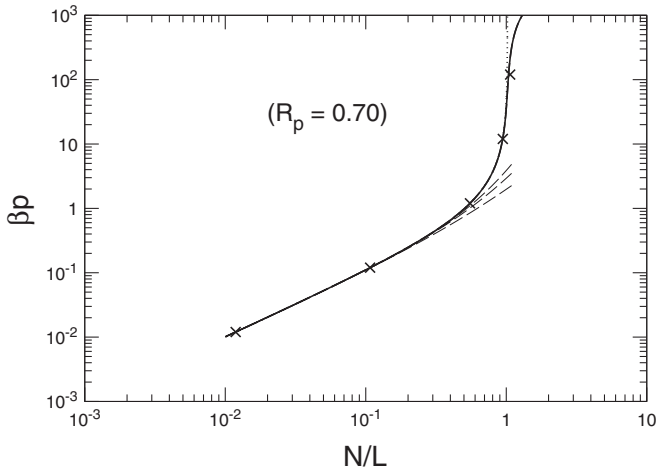

FIG. 3. Comparisons of linear pressure versus linear density plot for pore radius of $R_p = 0.70$ with Monte Carlo data. Monte Carlo data are denoted by a $\times$, and the statistical errors are less than the size of the symbols. The truncated virial density series are denoted by three dashed lines. The lowest line has $n_{max} = 2$, then $n_{max} = 3$ and $n_{max} = 4$. n_{max} is the maximum order of virial coefficients used in the truncated series. The truncated virial pressure series are denoted similarly by dotted, dashed, and solid lines. The lines for the three different pressure series are very close to each other and not distinguishable in the plots. A more quantitative comparison is given in Table II.

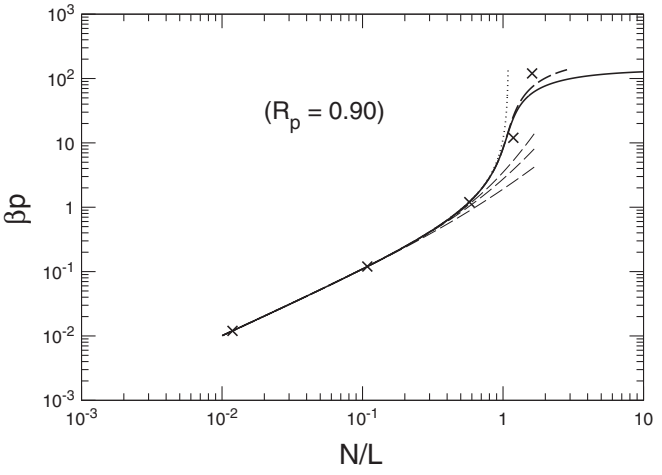

FIG. 4. Comparisons of linear pressure versus linear density plot for pore radius of $R_p = 0.90$ with Monte Carlo data. Monte Carlo data are denoted by a $\times$, and the statistical errors are less than the size of the symbols. The truncated virial density series are denoted by three dashed lines. The lowest line has $n_{max} = 2$, then $n_{max} = 3$ and $n_{max} = 4$. n_{max} is the maximum order of virial coefficients used in the truncated series. The truncated virial pressure series are denoted similarly by dotted, dashed, and solid lines.

$n_{max} = 4$. The truncated pressure series are denoted similarly by dotted, dashed, and solid lines. It appears that the truncated pressure virial series describes the Monte Carlo data better than the truncated density virial series with the same number coefficients; see Figs. 2–4. This should not be surprising, because the exact solution of the one-dimensional hard rod fluid has $B_n' = 0$, for $n \geqslant 3$ versus $B_n = 1$ for all n. One would then expect, hard spheres in very narrow pores would be similar. A truncated pressure series with all higher order set to zero would be better than similar truncated density series. As the pressure increases, the truncated pressure series must also fail, consistent with the comparisons shown. Since the higher order B_n' increases with $\hat{R} = R_p - 1/2$, failure of the truncated pressure series is more serious with $R_p = 0.90$ at higher pressures; see Fig. 4. On the whole, the truncated pressure virial series provides a very good description of the crossovers from the one-dimensional to narrow cylindrical pores at low and moderate pressures and densities. Observe that the truncation at $n_{max} = 3$ is already accurate over a wide range of pressure, density and pore sizes. This has the advantage that both B_2', B_3' are given analytically. For a more quantitative comparison, the nearest-neighbor longitudinal separation predictions and Monte Carlo data are presented in Table II.

V. REMARKS

In this paper, virial coefficients B_2 and B_3 were calculated analytically, and numerical quadrature was used for B_4. They were also used to obtain the virial pressure series coefficients, B_2', B_3', and B_4'. This allows us to compare the truncated virial density and pressure series expansions to accurate Monte Carlo data. Our comparisons shows that the truncated pressure virial series is accurate over a range of narrow pore widths, pressures, and densities. The truncated pressure series is much better than the corresponding truncated density virial series. This dramatic

TABLE II. Comparisons of linear pressure (βp) versus nearest-neighbor longitudinal separations $l(n_{max})$ of the truncated pressure virial series expansion predictions with Monte Carlo data. For three different pore radii of 0.52,0.70, and 0.90, the maximum order virial coefficients used are denoted by n_{max}. The uncertainty of the MC data is in the last digit with magnitude indicated by $(\cdots)$.

R_p	βp	$l(2)$	$l(3)$	$l(4)$	l(MC)
0.52	120.000	1.00813085	1.00813085	1.00813330	1.0081293 (5)
0.52	12.000	1.08313306	1.08313306	1.08313330	1.083132 (3)
0.52	1.200	1.83313328	1.83313328	1.83313330	1.833135 (8)
0.52	0.120	9.33313330	9.33313330	9.33313330	9.33310 (2)
0.52	0.012	84.33313330	84.33313330	84.33313330	84.33 (1)
0.70	120.000	0.96261062	0.96261062	0.98798509	0.938224 (2)
0.70	12.000	1.06044765	1.06044765	1.06298509	1.05804 (1)
0.70	1.200	1.81273135	1.81273135	1.81298509	1.8126 (1)
0.70	0.120	9.31295972	9.31295972	9.31298509	9.31295 (3)
0.70	0.012	84.31298256	84.31298256	84.31298509	84.313 (1)
0.90	120.000	0.16322831	0.42242831	0.92179176	0.62097 (2)
0.90	12.000	0.94426342	0.94685542	0.99679176	0.84457 (2)
0.90	1.200	1.74177221	1.74179813	1.74679176	1.7376 (2)
0.90	0.120	9.24629214	9.24629240	9.24679176	9.2462 (2)
0.90	0.012	84.24674182	84.24674183	84.24679176	84.24 (1)

difference is traced to the nature of the one-dimensional hard sphere fluid's exact solution. These results represent significant contributions to the long-standing problem of fluids in narrow pores.

ACKNOWLEDGMENTS

This work used the Extreme Science and Engineering Discovery Environment (XSEDE), which is supported by National Science Foundation Grant No. OCI-1053575.

[1] J. A. Barker, Aust. J. Phys. **15**, 127 (1962).
[2] E. D. Glandt, AIChE J. **27**, 51 (1981).
[3] P. E. Sokol, W. J. Ma, K. W. Herwig, W. M. Snow, Y. Wang, J. Koplik, and J. R. Banavar, Appl. Phys. Lett. **61**, 777 (1992).
[4] A. J. Post and D. A. Kofke, Phys. Rev. A **45**, 939 (1992).
[5] D. A. Kofke and A. J. Post, J. Chem. Phys. **98**, 4853 (1993).
[6] Q. Xin, I. Hiyne, and P. Siders, J. Chem. Soc., Faraday Trans. **90**, 973 (1994).
[7] K. E. Gubbins, M. Sliwinska-Bartkowiak, and S. H. Suh, Mol. Simul. **17**, 333 (1996).
[8] K. K. Mon and J. K. Percus, J. Chem. Phys. **112**, 3457 (2000).
[9] I. E. Kamenetskiy, K. K. Mon, and J. K. Percus, J. Chem. Phys. **121**, 7355 (2004).
[10] C. Forster, D. Mukamel, and H. A. Posch, Phys. Rev. E **69**, 066124 (2004).
[11] H. Kim, W. A. Goddard III, K. H. Han, C. Kim, E. K. Lee, P. Talkner, and P. Hänggi, J. Chem. Phys. **134**, 114502 (2011).
[12] K. K. Mon, J. Chem. Phys. **140**, 244504 (2014).
[13] M. J. Godfrey and M. A. Moore, Phys. Rev. E **89**, 032111 (2014).
[14] For a review and references see chapter 7 in Barry M. McCoy, *Advanced Statistical Mechanics* (Oxford University Press, Oxford, 2010). See also R. Kubo, *Statistical Mechanics* (North Holland, Amsterdam, 1965).
[15] For a review see A. J. Masters, J. Phys.: Condens. Matter **20**, 283102 (2008).
[16] J.-P. Hansen and I. R. McDonald, *Theory of Simple Liquids*, 3rd ed. (Academic, New York, 2006).
[17] J. E. Mayer and M. G. Mayer, *Statistical Mechanics* (Wiley, New York, 1940).
[18] F. H. Ree and W. G. Hoover, J. Chem. Phys. **41**, 1635 (1964); **40**, 2048 (1964).
[19] R. J. Wheatley, Phys. Rev. Lett. **110**, 200601 (2013).
[20] M. Bishop, Am. J. Phys. **51**, 1151 (1983).
[21] M. Luban and A. Baram, J. Chem. Phys. **76**, 3233 (1982).
[22] N. Clisby and B. M. McCoy, J. Stat. Phys. **122**, 15 (2006).
[23] M. Bishop, A. Masters, and J. H. R. Clarke, J. Chem. Phys. **110**, 11449 (1999).
[24] K. K. Mon and J. K. Percus, J. Chem. Phys. **110**, 2734 (1999).
[25] A. Bellemans, Physica **28**, 493 (1962); **28**, 617 (1962); **29**, 548 (1963); J. Stecki and S. Sokolowski, Mol. Phys. **39**, 343 (2006); S. Sokolowski and J. Stecki, Acta Phys. Pol. A **55**, 611 (1979); J. S. Rowlinson, Proc. R. Soc. London A **402**, 67 (1985); D. A. McQuarrie and J. S. Rowlinson, Mol. Phys. **60**, 977 (1987); For recent applications, see J. H. Yang, A. J. Schultz, J. R. Errrington, and D. A. Kofke, J. Chem. Phys. **138**, 134706 (2013).
[26] For a review and references see P. S. Burada, P. Hänggi, F. Marchesoni, G. Schmid, and P. Talkner, Chem. Phys. Chem. **10**, 45 (2009); see also L. D. Gelb, K. E. Gubbins, R. Radhakrishnan, and M. Sliwinska-Bartkowiak, Rep. Prog. Phys. **62**, 1573 (1999).
[27] W. H. Press, S. A. Teukolsky, W. T. Vetterling, and B. P. Flannery, *Numerical Recipes: The Art of Scientific Computing*, 3rd ed. (Cambridge University Press, New York, 2007).
[28] L. Tonks, Phys. Rev. **50**, 955 (1936).
[29] R. A. Dobbins, K. Mohammed, and D. A. Sullivan, J. Phys. Chem. Ref. Data **17**, 1 (1988).
[30] D. Frenkel and B. Smit, *Understanding Molecular Simulation* (Academic Press, New York, 2002).